Journal of Power Sources 252 (2014) 90–97

Contents lists available at ScienceDirect

Journal of Power Sources

journal homepage: www.elsevier.com/locate/jpowsour

Sulfurized activated carbon for high energy density supercapacitors

Yunxia Huang [a,b], Stephanie L. Candelaria [b], Yanwei Li [b], Zhimin Li [a], Jianjun Tian [b], Lili Zhang [b], Guozhong Cao [b,*]

[a] School of Advanced Materials and Nanotechnology, Xidian University, Xi'an 710071, China
[b] Department of Materials Science and Engineering, University of Washington, Seattle, WA 98195-2120, United States

HIGHLIGHTS

- Sulfur-modified activated carbon (AC) for supercapacitors was synthesized by the pyrolysis of sulfur flakes.
- Sulfur was introduced into the pores of AC through thiophenic sulfur functional groups.
- The incorporation of sulfur improves the electrical conductivity of the carbon network.
- The addition of sulfur can obviously increase the specific capacitance and energy density of AC.

ARTICLE INFO

Article history:
Received 22 August 2013
Received in revised form
21 November 2013
Accepted 2 December 2013
Available online 11 December 2013

Keywords:
Supercapacitor
Sulfur
Specific capacitance
Energy density
Activated carbon

ABSTRACT

Sulfurized activated carbon (SAC), made by coating the pore surface with thiophenic sulfur functional groups from the pyrolysis of sulfur flakes, were characterized and tested for supercapacitor applications. From X-ray photoelectron spectroscopy (XPS), the sulfur content in the SAC was found to be 2.7 at%. Electrochemical properties from potentiostatic and galvanostatic measurements, and electrochemical impedance spectroscopy (EIS) were used to evaluate the effect of sulfur on porous carbon electrodes. The SAC electrode exhibits better conductivity, and an obvious increase in specific capacitance that is almost 40% higher than plain activated carbons (ACs) electrode at a high current density of 1.4 A g^{-1}. The proposed mechanism for improved conductivity and capacitive performance due to the sulfur functional groups on ACs will be discussed.

1. Introduction

With the rapid consumption of fossil fuels, green and sustainable energy is going to play an increasingly important role and one of the greatest concerns is how the energy will be stored and deployed when needed. Currently, batteries, fuel cells, and supercapacitors are used as electric energy storage and conversion devices and extensive research is ongoing to improve these devices to meet energy needs. Supercapacitors, also called electrochemical capacitors or ultracapacitors, have attracted much attention because of their capability for pulsed power supply, long cycle life (>100,000 cycles), simple working principle, and fast charge propagation [1–3]. Related to the energy storage mechanism, supercapacitors can be categorized as either electric double layer capacitors (EDLCs) or pseudo-capacitors. The former is based on the accumulation of charges at the electrode/electrolyte interface, and therefore, capacitance is strongly dependent on the surface area of the electrode materials. The latter depends on the transfer of the electrons between the electrolyte ions and the surface of the electrode, i.e., a Faradaic reaction of the electrode materials [4–8].

Activated carbons (ACs) from different precursors and activation processes are widely used as electrode materials due to their chemical stability, large surface area, good electrical conductivity, greater ability for charge accumulation on the electrode/electrolyte interface, and low cost [6,9]. Activated carbon electrodes (ACEs) rely on their high surface area to form the electric double layer or promote pseudo-capacitive reactions. Although the specific surface area is an important parameter for carbon materials, the pore size distribution and pore morphology can also influence their electrochemical performance to a great extent [10]. However, the surface functionalized of ACs can also play an important role on the carbon electrode performance, particularly by affecting the wettability of the carbon surface and introducing pseudo-capacitance [6,11–16]. For example, oxygen functionalities present on the

* Corresponding author. Tel.: +1 206 616 9084; fax: +1 206 543 3100.
E-mail address: gzcao@u.washington.edu (G. Cao).

0378-7753/$ – see front matter © 2013 Elsevier B.V. All rights reserved.
http://dx.doi.org/10.1016/j.jpowsour.2013.12.004

carbon surface can induce electron acceptor characteristics into the carbon network to participate in Faradaic reactions, and thus, increase the specific capacitance of carbon in aqueous electrolytes [17–19]. However, they would be detrimental in organic electrolytes due to irreversible redox reactions between the electrolyte and oxygen [14]. Porous carbons modified with nitrogen functional groups or nitrogen dopants have attracted much interest because nitrogen functional groups contribute pseudo-capacitance through Faradaic reactions in both aqueous [20–22] and organic electrolytes [14,15]. Additionally, recent research demonstrated the capacitive performance of phosphorus-rich microporous carbons. The supercapacitors prepared by carbons enriched with phosphorus groups were stable at voltages higher than 1.3 V in H_2SO_4 aqueous electrolyte and have a uniquely high and stable capacitive performance through optimization of the porous structure [23].

Sulfur, similar to the heteroatoms oxygen, nitrogen, and phosphorus discussed above, possesses lone-pair electrons, which can also introduce pseudo-capacitance into the carbon network and/or influence pore size and structure to improve the specific capacitance of porous carbon. So far, little research on sulfur modified porous carbon used for EDLCs has been reported, but there are some researchers have used this material for other applications. For example, sulfur-functionalized carbon aerogels were prepared as receptor sites for metal catalysts [24]. Sulfur-doped microporous carbons were synthesized for the storage of hydrogen and carbon dioxide [25]. For EDLCs, Hasegawa et al. [26] produced macro/meso/microporous carbon monolith electrodes doped with sulfur from sulfonated poly(divinyl-benzene) (PDVB) prepared with concentrated H_2SO_4 and followed by carbonization and activation at 1000 °C. The resultant monolithic electrodes show high specific capacitance and good cycle performance in aqueous electrolyte owing to both the oxidation–reduction related to sulfur-containing groups and the hierarchical porous structure. Zhao et al. [27] used resorcinol and thioldiphenol as reactants to prepare mesoporous carbon doped with sulfide, sulfoxide, and sulfone functional groups. The specific capacitance of mesoporous carbon electrodes improved by 38% as compared to conventional ordered mesoporous carbon due to redox reactions and added electrons provided by the additional sulfone and sulfoxide species.

It is believed that sulfur-modified carbon will produce similar improvements in organic electrolyte. In addition to increasing capacitance, ACEs with sulfur modification might exhibit good electrochemical performance in organic electrolyte as the sulfur functional groups covering the surface may prevent undesirable chemical reactions between the impurities in AC and the electrolyte. In this research, sulfur-modified activated carbon (SAC) was prepared by coating the internal surface of AC with sulfur through thermal evaporation of pure sulfur flakes. Sulfur is coated on the surface of the highly porous carbon in order to introduce pseudo-capacitance, improve conductivity, and influence the structure of the pores. The SAC is then tested for supercapacitor applications. The chemical composition and pore structure are tested using scanning electron microscopy (SEM), X-ray photoelectron spectroscopy (XPS), and nitrogen sorption analysis. The electrochemical properties are characterized with cyclic voltammetry (CV), galvanic cycling (GC), and electrochemical impedance spectroscopy (EIS).

2. Experimental section

2.1. Materials synthesis

Commercially available activated carbon (AC) (Calgon Carbon Corporation, USA) and sulfur (reagent grade, flakes, ~100 mesh particle size, Sigma–Aldrich, Germany) with a weight ratio of 10:1 were mixed with a mortar and pestle and ground into uniform powders. Then the mixture was heat treated at 400 °C for 2 h to produce AC that is modified by sulfur (referred hereinafter to as SAC), with a heating rate of 5 °C min^{-1} under a nitrogen atmosphere with a flow rate of 10 ml min^{-1}. Due to part of S could be lost through evaporation during heating process, the SAC sample yield of the heating process is 79%.

2.2. Characterization

Surface morphologies of the cross sections of the AC and SAC samples were observed by field emission scanning electron microscopy (FESEM, JEOL JSM-7000) and the content of the samples was measured by energy dispersive X-ray spectroscopy (EDAX). Surface functional groups of the SAC sample were determined using XPS. Spectra were taken on a Surface Science Instruments S-probe spectrometer. The X-ray spot size for these acquisitions is approximately 800 μm with a take-off angle of 55°, corresponding to a sampling depth of approximately 50 Å. Data analyses was carried out using Service Physics ESCA Hawk 7 Data Analysis Software (Service Physics, Bend, OR).

Nitrogen sorption isotherms were analyzed by means of nitrogen sorption at −196 °C using a Quantachrome NOVA 4200e. Samples were degassed at 120 °C under vacuum for at least 6 h prior to measurement. The multipoint Brunauer–Emmett–Teller (BET) method is used to determine the total surface area. For the mesopore surface area, pore volume, and pore diameter, the Barrett–Joyner–Halenda (BJH) method is used. Micropore surface area and pore volume are determined using the t-method, and the micropore diameter is determined using the Dubinin–Astakhov (DA) method.

2.3. Electrochemical analysis

Electrodes for electrochemical measurements were prepared from the AC and SAC samples by first grinding the large particles into fine powders. Approximately 3 wt% of polytetrafluoroethylene (PTFE) was added as a binder. The mixture was rolled into sheets with a thickness of 0.07 mm and electrodes were punched out with a diameter of 10.2 mm. The materials loading rates of both the AC and SAC electrodes are 4.16×10^{-3} g cm^{-2}. A Celgard® porous film separates the electrodes and specially coated aluminum contacts were used to reduce the interfacial effect. To test the electrodes, a symmetrical two-electrode test cell was constructed with the AC or the SAC sample as the counter and reference electrode. The electrolyte used was tetraethylammonium tetrafluoroborate (TEATFB) in saturated 50/50 propylene carbonate-dimethylcarbonate. The electrode assembly was placed in a coin cell and electrolyte was added in an argon-rich environment. The samples were placed under vacuum three times to increase the penetration of the electrolyte into the pores.

Cyclic voltammograms (CVs) and galvanic cycles (GCs) were carried out using a Solartron 1287A with a voltage range between 0 and 2 V. The CVs were measured at scan rates of 10, 50, and 100 mV s^{-1} and the GCs at 0.07, 0.14, 0.7, and 1.4 A g^{-1}. EIS was performed using the Solartron 1287A in conjunction with a Solartron 1260FRA/impedance analyzer. An AC voltage amplitude of 10 mV and frequency range of 0.1 MHz–1 mHz was used for this scan. The specific capacitance of the single electrode in Farad per gram (F g^{-1}) is calculated from the discharge slope during galvanic cycling according to the following equation [23,28]:

$$C_{spec} = 4I\Delta t/\Delta Vm \quad (1)$$

where I is the discharge current in amps, Δt is the discharge time in seconds, ΔV is the discharge voltage in volts, and m is the total mass

of the active materials in both electrodes given in grams. The specific capacitance based on the BET surface area is calculated using Eqn. (2) [16]:

$$C_{BET} = C_{spec}\ (F\ g^{-1})/S_{BET}\ (m^2\ g^{-1}) \quad (2)$$

Where S_{BET} is the specific surface area of the electrode. Energy density in Watt-hours per kilogram (Wh kg^{-1}) and power density in Watts per kilogram (W kg^{-1}) are calculated using the following equations [23]:

$$E = (C_{spec}{}^{*}\Delta V^2)/2 \quad (3)$$

$$P = [(I^{*}\Delta V)/2^{*}m] \quad (4)$$

3. Results and discussion

3.1. Composition and structure

XPS was used to determine the chemical state of sulfur in the carbon network. The results from XPS are shown in Table 1. Since no special handling or pretreatment was performed, O_2 and H_2O from the ambient environment were probably adsorbed on the surface of the samples. Additionally, oxygen is also a common impurity in the AC. The sulfur content of the SAC sample is 2.7 at%, indicative of the presence of sulfur in the AC after heat-treatment.

Fig. 1 shows high resolution XPS spectra of C 1s and S 2p for the SAC sample. As seen in Fig. 1a, the asymmetric C1s spectrum could be fit with three peaks. The peak observed at about 285.0 eV is consistent with graphitic sp^2 carbon [25], which indicates the structure of carbon in the sample. The peaks at 286.3 eV represents carbon bound to one oxygen or sulfur by a single bond (e.g., C–O, C–S) [29,30]. The 289.3 eV peak are derived from O–C=O bond [29,31]. The XPS spectrum for S 2p shown in Fig. 1b indicates that S is incorporated in the graphitic ring structure. The S 2p core level line exhibits S $2p_{3/2}$ and S $2p_{1/2}$ signals at 164.2 eV and 165.4 eV, respectively, as well as a trace peak at 168.5 eV. The S $2p_{3/2}$ and S $2p_{1/2}$ peaks constrained by 2:1 concentration ratio and 1.2 eV binding energy separation correspond to spin-orbital splitting of thiophenic sulfur atoms incorporated into graphite structure, i.e. sulfur dominated in the carbon framework through the formation of the C–S bond [24,29,32]. The trace peak at 168.5 eV is located at the expected position for sulfone groups [27,29].

Fig. 2a and b show SEM images of the cross-section of the unmodified and S-modified AC samples, respectively. It can be seen that the surface morphologies of the AC and SAC samples have no obvious difference and macro-pores are visible in the images. The SAC sample still retains the porous structure after modification with sulfur. The elemental mappings for C and S from the same area of the SAC sample are shown in Fig. 2c and d. The images indicate uniform presence of sulfur throughout the sample. The sulfur content in the SAC sample derived from the EDAX analysis shown in Table 1 is close to the value obtained from XPS analysis, further implying the sulfur functional groups are homogenously distributed in the SAC sample.

Table 1
Chemical composition (at %) from EDAX and XPS.

Element	Composition (at %)		
	AC sample (from EDAX)	SAC sample (from EDAX)	SAC sample (from XPS)
C	88.7	93.9	87.3
O	11.4	3.4	10.0
S	–	2.7	2.7

Fig. 3 shows the nitrogen adsorption/desorption isotherms of the AC and SAC samples. The sorption isotherms have similar shapes and can be classified as type IV, which has an obvious capillary condensation step at high relative pressures. A hysteresis loop can be observed in both the isotherms, indicating the existence of similar sized mesopores in both samples. However, in the SAC sample the desorption isotherm diverged at low relative pressures (about $p/p_0 < 0.1$), an indication of a structure change or a chemical alteration in the meso- and micropore regions [33]. On the other hand, the similarities of both curves suggest the structure of the porous of carbon is still present [15].

Table 2 shows the corresponding data associated with the surface area, pore volume and pore diameter. It can be seen that the AC sample has a total surface area of 1094 $m^2\ g^{-1}$, and after coating with sulfur the total surface area decreases to 987 $m^2\ g^{-1}$ for the SAC sample. At the same time, the meso- and micropore surface areas decrease from 292 and 526 $m^2\ g^{-1}$ for the AC sample to 272 and 458 $m^2\ g^{-1}$ for the SAC sample, respectively. However, this result shows the sulfur did coat the surface of the pores.

Fig. 4a and b show the pore size distribution curves of the AC and SAC samples calculated by using the BJH model and DA method, respectively. A small difference in the mesopore volume between the AC and SAC samples is seen, with the inset in Fig. 4a clearly showing the difference of the mesopores size distribution. The pore size distribution maxima of the AC sample are centered at ~4.8, ~7.8 and ~13.0 nm, whereas those in the SAC sample shift to ~9.7, ~13.1 and ~15.8 nm. Furthermore, the pore size distribution of the SAC sample is rather broad as compared to the AC sample. The mesopore volume decrease and pore size change of the SAC sample are caused by the micropores partly growing to form mesopores during heating treatment and then the resultant mesopores filling with sulfur groups during the sulfur processing. However, the micropore volume of the SAC sample has an obvious decrease as shown in Fig. 4b, which is caused by the micropores filling with sulfur groups. The best observation for the filling of the meso- and micropores is to measure the pore volume. Table 2 shows both meso- and micropores volumes clearly decrease after the sulfur functionalized, though there is no appreciable change in the meso- and micropore peak size. This type of hierarchical surface morphologies with well developed pore structures are advantageous for energy storage applications since large pore channels permit rapid electrolyte transport, while the small pores provide more active sites for chemical reactions [34].

3.2. Electrochemical analysis

The CV curves taken at a scan rate of 10 mV s^{-1} are shown in Fig. 5a. The fairly rectangular shape of the AC and SAC samples indicates capacitive behavior from the formation of an electric double layer. Additionally, both samples exhibit a strong peak at 2 V potential, which indicates that pseudo-capacitance is present [15]. Table 1 compared the content of oxygen in the ACs with and without sulfur modification and it was evident that the oxygen content was significantly reduced after introducing sulfur. Therefore, for the AC sample the pseudo-capacitance results from oxygen on the surface of the porous carbon, while that in the SAC sample is mainly from sulfur in addition to oxygen. Oxygen is detrimental in organic electrolytes due to irreversible redox reactions between the electrolyte and oxygen [14]. However, the sulfur functional groups covering the sample surface may prevent the undesirable chemical reactions. Fig. 5b and c show CV curves taken at a wide range of scan rates. It can be seen that the curves of the SAC sample retain rectangular shaped current voltage response even at 100 mV s^{-1}, whereas in the AC sample the rectangular shapes gradually deteriorated with increasing scan rates.

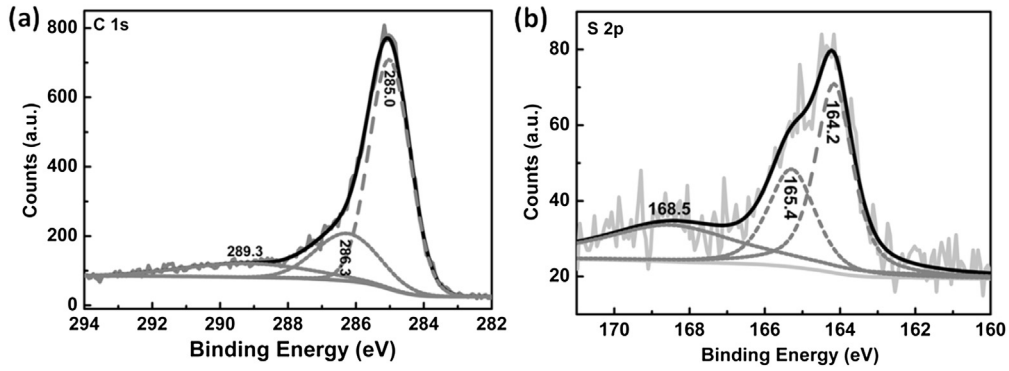

Fig. 1. XPS spectra of C 1s (a) and S 2p (b) for the SAC sample.

The exact mechanism for how sulfur introduces pseudo-capacitance in the SAC sample is unknown at this time. According to XPS analysis, in the SAC sample sulfur is incorporated into carbon framework through the formation of C–S and C–SO_2–C bonds to produce the similar thiophene and sulfone structure. Sulfone group is a possible by-product of the pyrolysis procedure. The additional sulfone species could participate in Faradaic reactions and improve the specific capacitance of carbon in aqueous electrolytes [27]. However, it would be detrimental in organic electrolytes due to irreversible redox reactions between the electrolyte and oxygen [14]. The increased capacitance of the SAC sample is mainly attributed to the thiophene-like functional groups. In this structure, it can be proposed that a lone electron pair among the sulfur atom *p*-orbital overlaps with π-orbitals of the graphite sp^2 hybridization to form an extended π-system with a filled valence band, resulting in an increased conductivity due to delocalized electrons along the conjugated backbones of carbon. On the other hand, it is believed that pseudo-capacitance arises from Faradaic reaction induced by another lone electron pair from the sulfur groups interacting with the cations in the electrolyte [14,27]. The following are possible reactions that could be taking place on the sulfur-functionalized carbon surface:

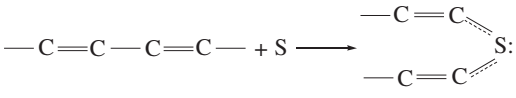

(5)

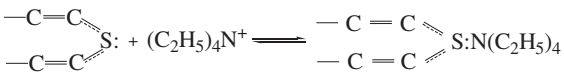

(6)

Galvanic cycling further illustrates pseudo-capacitance and resistance in the samples. Fig. 6a–d shows the GC curves measured

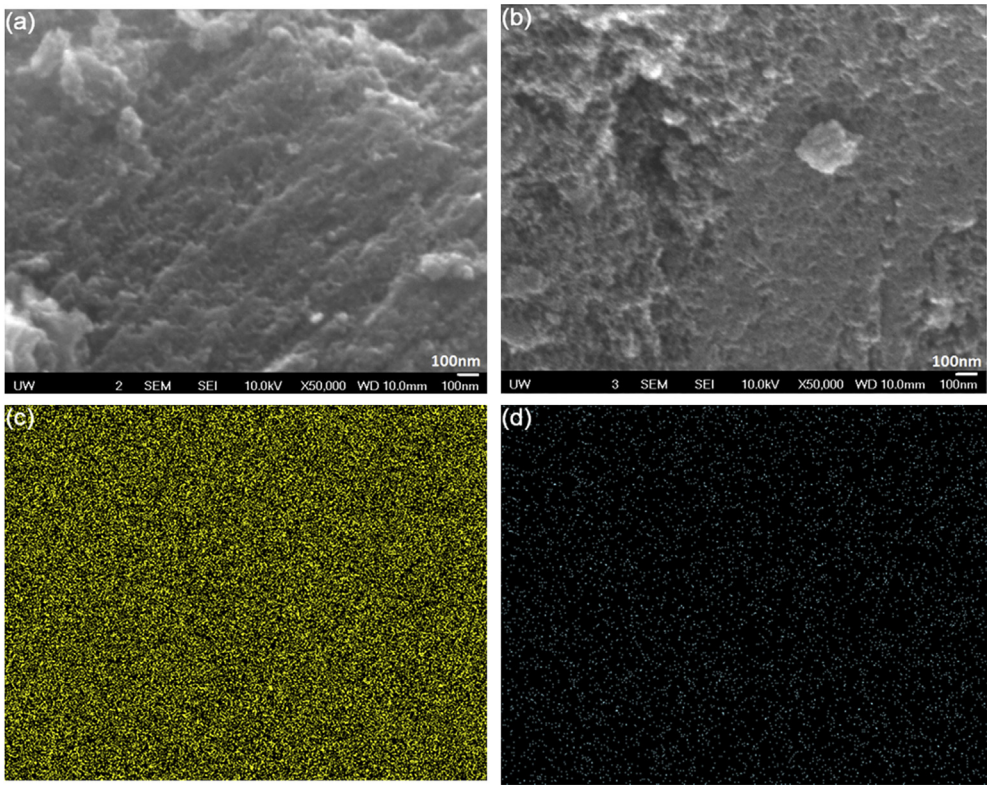

Fig. 2. Typical SEM images of (a) AC and (b) SAC samples and the elemental mappings of (c) carbon and (d) sulfur from the SAC sample.

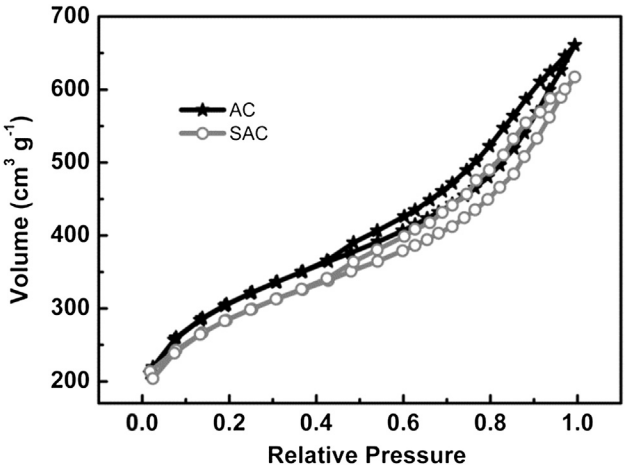

Fig. 3. Nitrogen adsorption/desorption isotherms for the AC and SAC samples.

Table 2
The pore structure parameters of the AC and SAC samples.

Sample	S^*_{BET} ($m^2\ g^{-1}$)	S_{meso} ($m^2\ g^{-1}$)	S_{micro} ($m^2\ g^{-1}$)	V^*_{meso} ($cm^3\ g^{-1}$)	V_{micro} ($cm^3\ g^{-1}$)	D^*_{meso} (nm)	D_{micro} (nm)
AC	1094	292	526	0.647	0.286	3.2	1.6
SAC	987	272	458	0.614	0.249	3.2	1.6

S_x – surface area, V_x – pore volume, D_x – pore diameter.

at 0.07, 0.14, 0.7 and 1.4 A g^{-1}, respectively. It is noted that the discharge time of the SAC sample is higher than that of the AC sample at the same current density. Furthermore it is found from the charge and discharge curves of the SAC sample that smaller potential drop (IR drop) at the beginning of the discharge process is observed at 0.7 and 1.4 A g^{-1} as compared to the AC sample, indicating that the SAC electrode has better conductivity [35]. In addition, all samples exhibit non-linear charging behavior characteristic of pseudo-capacitive reactions. However, the linear discharge behavior of the samples can be attributed to a charge selective Faradaic reaction, which results from the oxygen containing functional groups in the samples under the chosen voltage range [34].

The specific capacitance is calculated from the discharge slopes of these curves using Eqn. (1). The results are shown in Table 3. The SAC samples exhibit higher specific capacitance. At current densities of 0.07–1.4 A g^{-1}, the specific capacitance values for the AC sample are found to be 72.7–44.6 F g^{-1}. A higher current density leads to a lower specific capacity. Similarly, at the same current density the specific capacitance values for the SAC sample are in the range of 82.3–62.0 F g^{-1}. Also, the specific capacitance decreases with increasing current density for both the AC and SAC samples, which results from the electrode polarization. Table 3 also shows the capacitance normalized to surface area according to eqn. (2). These values are relatively lower as well, which is caused by the low mesopore surface area in these samples. Without adequate mesopores in the activated carbon, penetration of the electrolyte is limited by pore apertures that can be much smaller than the average pore sizes listed in Table 2 and may be too small to allow the electrolyte ions to pass. The total accessible surface area is most likely much lower than the total surface area measured by nitrogen sorption, as reported and discussed in literature [14]. However, the SAC sample exhibits higher capacitance per unit mass, surface area and volume, which can be attributed to the sulfur on the surface of the carbon.

Long cyclic stability is one of the most important requirements for practical competence of supercapacitor devices. The cyclic specific capacitance plot of the AC and SAC samples for 200 cycles at current density of 0.7 A g^{-1} are shown in Fig. 7. From the data plot, it can be ascertained that specific capacitance of the SAC sample is still higher than the AC sample after 200 cycles, though the specific capacitance in both the samples degrades slightly with increasing cycle numbers. In addition, both the samples possess similar capacitive retention, which maintain 90% capacitance after 200 cycles. Further, for both the samples the specific capacitance retention keeps approximately constant during the 140–200 charge–discharge cycles. These performance data suggest excellent higher rate electrochemical performance of the SAC sample as compared to the AC sample.

Because the energy density of supercapacitors is proportional to the specific capacitance according to eqn. (3), higher energy density for the SAC sample results from the better specific capacitance. The improvement in energy density can be clearly seen in the Ragone plot as shown in Fig. 8. The curve of the SAC sample is positioned on the right side of the AC sample curve along the *X*-axis, showing the SAC sample has better energy and power performance than the AC sample. As the power density increased, reduction in energy density was less pronounced in the SAC sample than in the AC sample. The energy and power density used for the Ragone plot were calculated from GC curves and eqn. (3) and (4).

EIS can provide insight into how the sulfur modification affects the performance of the sample. The Nyquist plots of the AC and SAC samples are shown in Fig. 9. For both the samples, the complex-plane impedance plots are simulated by using the equivalent circuit as shown in the inset of Fig. 9. The EIS data are interpreted based on proposed equivalent circuits using a suitable fitting procedure elaborated by ZView (Solartron's complex non-linear least

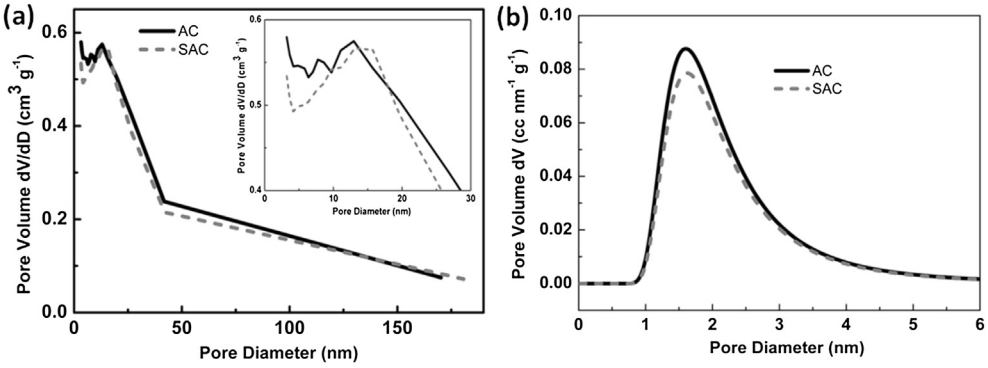

Fig. 4. Pore size distributions: (a) BJH mesopore distribution, the inset shows the difference of the mesopores size distribution; (b) DA micropore distribution.

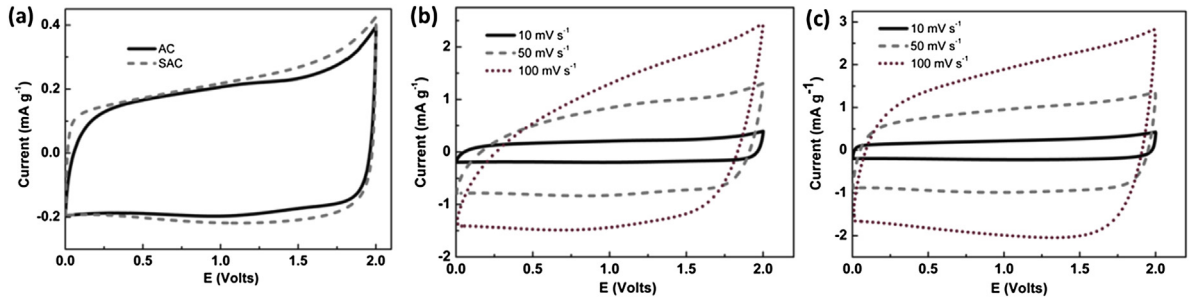

Fig. 5. (a) Comparison of CV curves of the AC and SAC samples at 10 mV s^{-1}; CV curves of (b) AC sample and (c) SAC sample at different scan rates.

square (CNLS) fitting application). It can be seen that a good agreement between the experimental and simulated data is confirmed. The impedance plots of both the samples show almost similar profiles with one semicircle at the high frequency region followed by a linear part in the low frequency region. It is known that a slope of the linear part at low frequency close to 90° along the imaginary axis Z″ is a characteristic of ideally polarizable electrode, while the high frequency large semicircle is indicative of the high interfacial charge-transfer resistance due to the poor electrical conductivity of electrode materials [35–38]. The intersecting part with the real axis (Z′) in the high frequency region is the resistance resulting from the electrolyte resistance, the contact resistance between the carbon particles and at the interface between the current collector and carbon electrode, and the intrinsic resistance of the current collectors and the carbon [39]. As seen in Fig. 9, the SAC sample has a slight deviation from the straight line along the Z″ axis and a smaller semicircle as compared to the AC sample, implying good capacitive performance and lower interfacial charge-transfer resistance in the SAC sample.

The equivalent series resistance (ESR) is a measure of conductivity of an electrode material [39], and was obtained by the data fitting using the equivalent circuit from the inset in Fig. 9. The electrolyte resistance (R_s) is constant for given electrolyte [40]. The non-ideality or frequency dispersion has been described widely by the constant phase element (CPE) that is an empirical distributed element [41]. CPE_1: $Y = Y_p\,(j\omega)^{\alpha}$ in parallel with the charge transfer resistance (R_{ct}) is modeling the high frequency semicircle, which signifies charge transfer process in the electrode–electrolyte interfaces, and could be influenced by roughness, pores, or grow defects [42–44]. The R_{ct} is in series with CPE_2: $Y = Y_q\,(j\omega)^{\beta}$, and it is related with the electrolyte–aluminum interface connected to the charge transfer resistance in the double layer capacitance [45–49]. Here Y_p and Y_q are the frequency independent constants, $j^2 = (-1)$, ω is the angular frequency, and the exponents α and β are between $0 < \alpha, \beta < 1$ [45]. For the AC and SAC samples, the values of α are 0.4949 and 0.5639, and the β values are 0.6234 and 0.803, respectively. The calculated ESR values of the AC and SAC samples are 10.6 and 8.2 Ω, respectively. The reduced charge transfer resistance for the SAC electrode can be attributed to the enhanced conductivity from the sulfur-functionalized support, as demonstrated by Eqn. (5). Therefore, the EIS data indicate that the electrical conductivity of the SAC electrode is obviously improved by

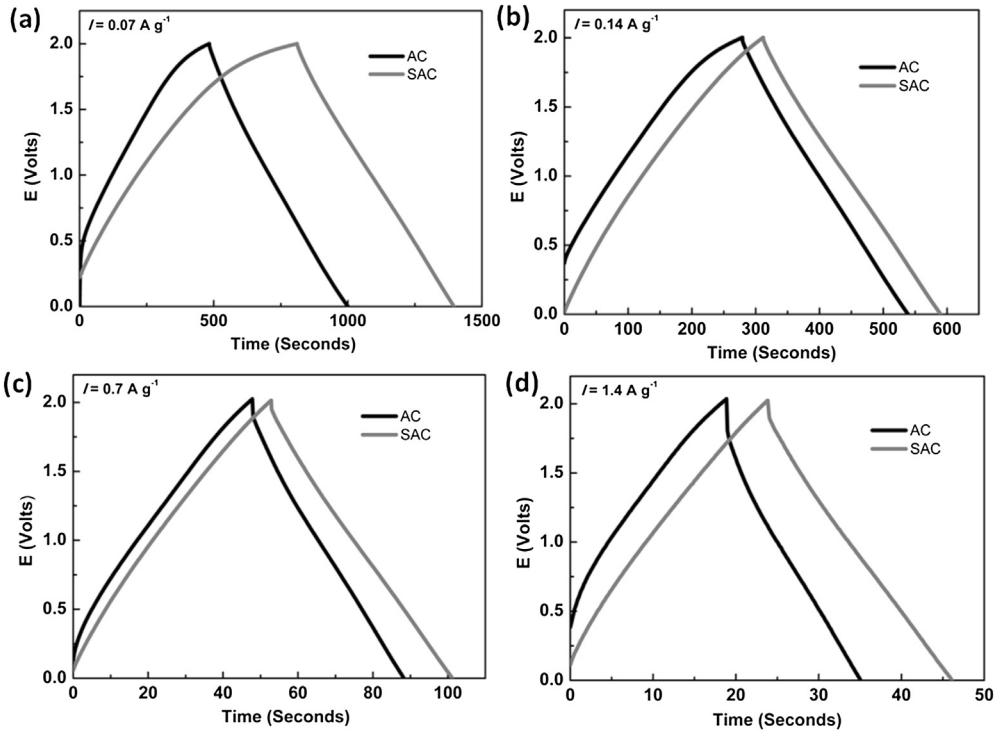

Fig. 6. GC curves of the AC and SAC samples at different current density: (a) 0.07 A g^{-1}; (b) 0.14 A g^{-1} (c) 0.7 A g^{-1}; (d) 1.4 A g^{-1}.

Table 3
Capacitance based on mass, surface area and volume.

Current density (A g^{-1})	Specific capacitance (F g^{-1})		Capacitance based on total surface area (F m^{-2})		Volumetric capacitance (F cm^{-3})	
	AC	SAC	AC	SAC	AC	SAC
0.07	72.7	82.3	0.066	0.083	39.5	48.3
0.14	73.1	78.2	0.067	0.079	39.7	46.0
0.7	56.2	67.4	0.051	0.068	30.5	39.6
1.4	44.6	62.0	0.041	0.063	24.2	36.4

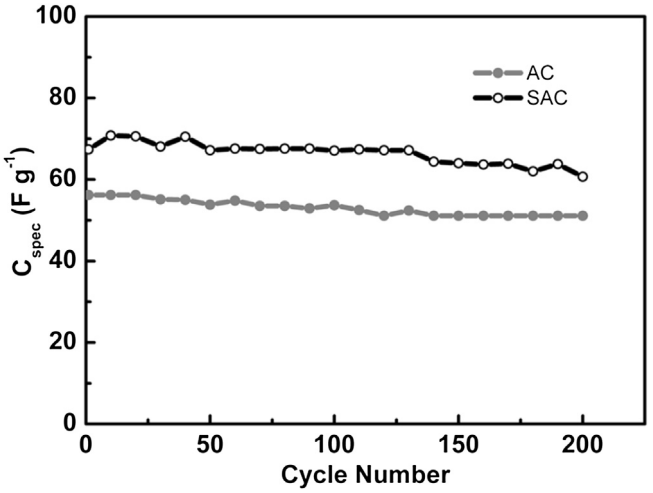

Fig. 7. Specific capacitance of the AC and SAC samples with cycle number at current density of 0.7 A g^{-1}, derived from the GCs study.

the presence of thiophenic sulfur functional groups, leading to enhanced electrochemical properties.

On the other hand, the capacitance could be evaluated from the low frequency data of the EIS spectra by the Eq. (7) [50]:

$$C = -1/(2\pi f Z^{\wedge\prime\prime}) \quad (7)$$

There f represents frequency and Z'' is the imaginary part of the Z. The specific capacitances of the AC and SAC samples are 11.7 F g^{-1} and 14.3 F g^{-1}, respectively. The specific capacitance value from EIS would be smaller than the value calculated from the CV curves at

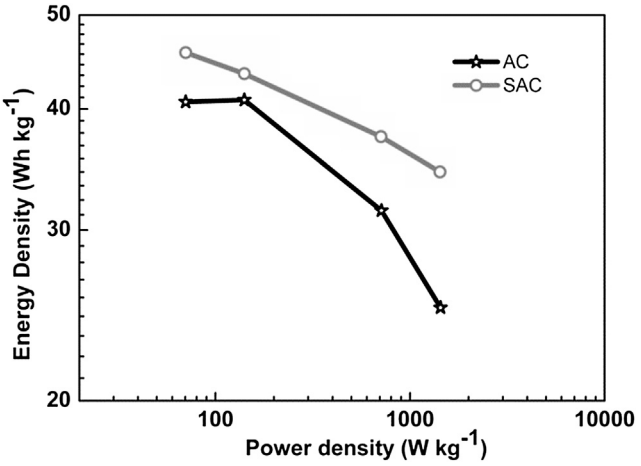

Fig. 8. The Ragone plots of the energy density and power density of the AC and SAC samples.

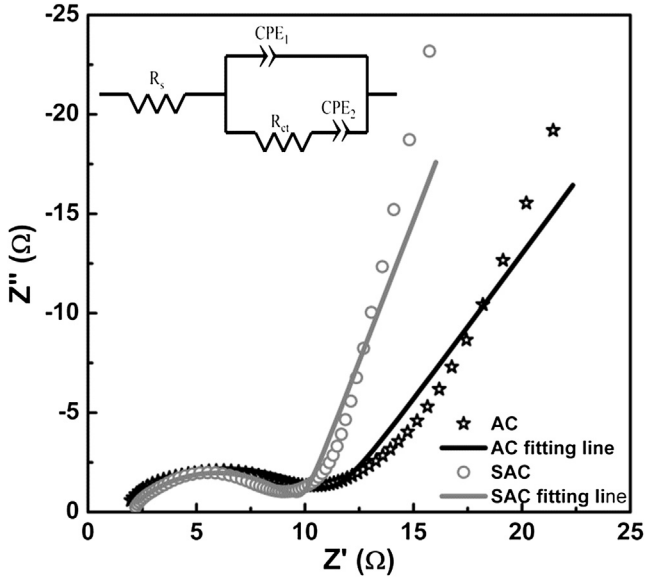

Fig. 9. EIS of the AC and SAC samples, the inset is equivalent circuit.

low scanning rate due to the influence of redox hysteresis on the charge transfer resistance [51].

4. Conclusions

The pyrolytic decomposition of sulfur flakes has been demonstrated to be a viable method to modify the surface chemistry of the AC. Modification of AC with sulfur has been proved to increase the capacitance and energy density of electrodes for supercapacitor applications. The sulfur introduces Faradaic reactions, which contributes to the capacitance that is already present from electric double-layer formation. The SAC electrodes shows high specific capacitance that is an almost 40% enhancement at a current density of 1.4 A g^{-1} and still retains electric double-layer formation even at a high scan rate, owing to the improved hierarchical pore structure which allows an effective transport of electrolyte ions. Furthermore, the SAC shows better conductivity as compared to unmodified AC.

Acknowledgments

This work is supported in part by National Science Foundation (CMMI-1030048) and the Fundamental Research Funds for the Central University of China (K5051205006). Yunxia Huang would like to acknowledge the fellowship from China Scholarship Council (CSC) and the NESAC/BIO (EB-002027).

References

[1] M. Winter, R.J. Brodd, Chem. Rev. 104 (2004) 4245–4269.
[2] A. Burke, J. Power Source 91 (2000) 37–50.
[3] J.R. Miller, P. Simon, Science 321 (2008) 651–652.
[4] B.E. Conway, Electrochemical Supercapacitors: Scientific Fundamentals and Technological Applications, Kluwer Academic Plenum Publisher, New York, 1999.
[5] K.S. Kim, S.J. Park, J. Electroanal. Chem. 673 (2012) 58–64.
[6] Q.F. Zhang, E. Uchaker, S.L. Candelaria, G.Z. Cao, Chem. Soc. Rev. 42 (2013) 3127–3171.
[7] S.L. Candelaria, Y.Y. Shao, W. Zhou, X.L. Li, J. Xiao, J.G. Zhang, Y. Wang, J. Liu, J.H. Li, G.Z. Cao, Nano Energy 1 (2012) 195–220.
[8] S.L. Candelaria, R. Chen, Y.H. Jeong, G.Z. Cao, Energy Environ. Sci. 5 (2012) 5619–5637.
[9] E. Frackowiak, Phys. Chem. Chem. Phys. 9 (2007) 1774–1785.

[10] B.B. Garcia, A.M. Feaver, Q.F. Zhang, R.D. Champion, G.Z. Cao, T.T. Fister, K.P. Nagle, G.T. Seidler, J. Appl. Phys. 104 (2008), 014305-1-9.
[11] A.G. Pandolfo, A.F. Hollenkamp, J. Power Sources 157 (2006) 11–27.
[12] M. Seredych, D. Hulicova-Jurcakova, G.Q. Lu, T.J. Bandosz, Carbon 46 (2008) 1475–1488.
[13] C. Largeot, C. Portet, J. Chmiola, P.L. Taberna, Y. Gogotsi, P. Simon, J. Am. Chem. Soc. 130 (2008) 2730–2731.
[14] S.L. Candelaria, B.B. Garcia, D.W. Liu, G.Z. Cao, J. Mater. Chem. 22 (2012) 9884–9889.
[15] B.B. Garcia, S.L. Candelaria, G.Z. Cao, J. Mater. Sci. 47 (2012) 5996–6004.
[16] S. Sepehri, B.B. Garcia, Q.F. Zhang, G.Z. Cao, Carbon 47 (2009) 1436–1443.
[17] H.A. Andreas, B.E. Conway, Electrochim. Acta 51 (2006) 6510–6520.
[18] M.A. Montes-Moran, D. Suarez, J.A. Menendez, A.E. Fuente, Carbon 42 (2004) 1219–1225.
[19] K. Jurewicz, K. Babel, A. Ziolkowski, H. Wachowska, Electrochim. Acta 48 (2003) 1491–1498.
[20] D. Hulicova-Jurcakova, M. Kodama, S. Shiraishi, H. Hatori, Z.H. Zhu, G.Q. Lu, Adv. Funct. Mater. 19 (2009) 1800–1809.
[21] D. Hulicova, J. Yamashita, Y. Soneda, H. Hatori, M. Kodama, Chem. Mater. 17 (2005) 1241–1247.
[22] F. Beguin, K. Szostak, G. Lota, E. Frackowiak, Adv. Mater. 17 (2005) 2380–2384.
[23] D. Hulicova-Jurcakova, A.M. Puziy, O.I. Poddubnaya, F. Suarez-Garcia, J.M.D. Tascon, G.Q. Lu, J. Am. Chem. Soc. 131 (2009) 5026–5027.
[24] W.S. Baker, J.W. Long, R.M. Strouda, D.R. Rolison, J. Non-Cryst. Solids 350 (2004) 80–87.
[25] Y.D. Xia, Y.Q. Zhu, Y. Tang, Carbon 50 (2012) 5543–5553.
[26] G. Hasegawa, M. Aoki, K. Kanamori, K. Nakanishi, T. Hanada, K. Tadanaga, J. Mater. Chem. 21 (2011) 2060–2063.
[27] X.C. Zhao, Q. Zhang, C.M. Chen, B.S. Zhang, S. Reichea, A.Q. Wang, T. Zhang, R. Schlogl, D.S. Su, Nano Energy 1 (2012) 624–630.
[28] Z.B. Lei, Z.W. Chen, X.S. Zhao, J. Phys. Chem. C 114 (2010) 19867–19874.
[29] S.R. Kelemen, M. Afeworki, M.L. Gorbaty, M. Sansone, P.J. Kwiatek, C.C. Walters, H. Freund, M. Siskin, Energy Fuels 21 (2007) 1548–1561.
[30] H.X. Wang, H. Zhou, A. Gestos, J. Fang, H. Niu, J. Ding, T. Lin, Soft Matter 9 (2013) 277–282.
[31] Z. Konya, I. Vesselenyi, K. Niesz, A. Kukovecz, A. Demortier, A. Fonseca, J. Delhalle, Z. Mekhalif, J.B. Nagy, A.A. Koos, Z. Osvath, A. Kocsonya, L.P. Biro, I. Kiricsi, Chem. Phys. Lett. 360 (2002) 429–435.
[32] S. Glenis, A.J. Nelson, M.M. Labes, J. Appl. Phys. 86 (1999) 4464–4466.
[33] G.Q. Lu, X.S. Zhao, Nanoporous Materials Science and Engineering, Imperial College Press, London, 2004.
[34] B.B. Garcia, S.L. Candelaria, D.W. Liu, S. Sepheri, J.A. Cruz, G.Z. Cao, Renewable Energy 36 (2011) 1788–1794.
[35] W. Xiong, M.X. Liu, L.H. Gan, Y.K. Lv, Y. Li, L. Yang, Z.J. Xu, Z.X. Hao, H.L. Liu, L.W. Chen, J. Power Sources 196 (2011) 10461–10464.
[36] W. Sugimoto, H. Iwata, K. Yokoshima, Y. Murakami, Y. Takasu, J. Phys. Chem. B 109 (2005) 7330–7338.
[37] J.T. Zhang, J.W. Jiang, X.S. Zhao, J. Phys. Chem. C 115 (2011) 6448–6454.
[38] Y.R. Nian, H. Teng, J. Electrochem. Soc. 149 (2002) A1008–A1014.
[39] S.K. Meher, G.R. Rao, J. Power Sources 215 (2012) 317–328.
[40] C. Kim, K.S. Yang, Appl. Phys. Lett. 83 (2003) 1216–1218.
[41] H.K. Song, H.Y. Hwang, K.H. Lee, L.H. Dao, Electrochim. Acta 45 (2000) 2241–2257.
[42] S.K. Meher, P. Justin, G.R. Rao, Electrochim. Acta 55 (2010) 8388–8396.
[43] C.C. Hu, K.H. Chang, T.Y. Hsu, J. Electrochem. Soc. 155 (2008) F196–F200.
[44] O.M.S. Quintero, W.A. Chaparro, L. Ipaz, J.E.S. Barco, F.E. Beltrán, G. Zambrano, Mater. Res. 16 (2013) 204–214.
[45] C. Liu, Q. Bi, A. Matthews, Corros. Sci. 43 (2001) 1953–1961.
[46] J.H. Lee, S.H. Ahn, J.G. Kim, Surf. Coat Technol. 190 (2005) 417–427.
[47] Y.Y. Chang, D.Y. Wang, Surf. Coat Technol. 188–189 (2004) 478–483.
[48] S.H. Ahn, J.H. Yoo, Y.S. Choi, J.G. Kim, J.G. Han Surf, Coat Technol. 162 (2003) 212–221.
[49] D.K. Merl, P. Panjan, M. Čekada, M. Maček, Electrochim. Acta 49 (2004) 1527–1533.
[50] J. Wang, Y. l. Xu, X. hen, X.F. Sun, Combust. Sci. Technol. 67 (2007) 2981–2985.
[51] R. Hass, J. García-Canadas, G. Garcia-Belmonte, J. Electroanal. Chem. 577 (2005) 99–105.